

# Collide and Conquer: Constraints on Simplified Dark Matter Models using Mono- $X$ Collider Searches

A. J. Brennan,<sup>a,1</sup> M. F. McDonald,<sup>a</sup> J. Gramling<sup>b</sup> and T. D. Jacques<sup>c</sup>

<sup>a</sup>*The University of Melbourne, Parkville 3010, Australia*

<sup>b</sup>*Université de Genève, Quai E. Ansermet 24, 1211 Genève 4, Switzerland*

<sup>c</sup>*SISSA/ISAS, via Bonomea 265, 34136 Trieste, Italy*

*E-mail:* [amelia.brennan@coepp.org.au](mailto:amelia.brennan@coepp.org.au), [millie.mcdonald@coepp.org.au](mailto:millie.mcdonald@coepp.org.au),  
[johanna.gramling@cern.ch](mailto:johanna.gramling@cern.ch), [thomas.jacques@sissa.it](mailto:thomas.jacques@sissa.it)

ABSTRACT: The use of simplified models as a tool for interpreting dark matter collider searches has become increasingly prevalent, and while early Run II results are beginning to appear, we look to see what further information can be extracted from the Run I dataset. We consider three ‘standard’ simplified models that couple quarks to fermionic singlet dark matter: an  $s$ -channel vector mediator with vector or axial-vector couplings, and a  $t$ -channel scalar mediator. Upper limits on the couplings are calculated, and compared across three alternate channels, namely, mono-jet, mono- $Z$  (leptonic) and mono- $W/Z$  (hadronic). The strongest limits are observed in the mono-jet channel, however the computational simplicity, and absence of significant  $t$ -channel model width effects, in the mono-boson channels make these a straightforward and competitive alternative. We also include a comparison with relic density and direct detection constraints.

---

<sup>1</sup>Corresponding author.

---

21	<b>Contents</b>	
22	<b>1 Introduction</b>	<b>2</b>
23	<b>2 Simplified Model Phenomenology</b>	<b>3</b>
24	2.1 Model Descriptions	3
25	2.2 The Mono- $X + E_T^{\text{miss}}$ Signature	4
26	2.3 Mass and Coupling Points	5
27	2.4 Treatment of the width	5
28	<b>3 Recasting mono-<math>X</math> constraints</b>	<b>7</b>
29	3.1 Signal Simulation	8
30	3.1.1 Parton Matching Scheme	9
31	3.2 Mono-jet Constraints	9
32	3.3 Mono- $Z(\text{lep})$ Constraints	10
33	3.4 Mono- $W/Z(\text{had})$ Constraints	11
34	<b>4 Results and Discussion</b>	<b>12</b>
35	4.1 Limits on the coupling $\sqrt{g_q g_\chi}$	12
36	4.1.1 Mono-jet channel	13
37	4.1.2 Mono- $Z(\text{lep})$ channel	14
38	4.1.3 Mono- $W/Z(\text{had})$ channel	14
39	4.2 Comparison with Relic Density Constraints	15
40	4.3 Comparison with Direct Detection Constraints	15
41	<b>5 Conclusion</b>	<b>21</b>
42	<b>6 Acknowledgements</b>	<b>22</b>
43	<b>A Limit setting strategy</b>	<b>22</b>
44	A.1 Nominal Values	22
45	A.2 Uncertainty Estimation	22
46	<b>B Validation of signal simulation and event selection procedures</b>	<b>23</b>
47	B.1 Monojet Channel	23
48	B.2 Mono- $Z(\text{lep})$ Channel	24
49	B.3 Mono- $W/Z(\text{had})$ Channel	25

---

# 1 Introduction

Simplified models have emerged as a powerful tool for the interpretation of collider, direct and indirect detection signals of dark matter (DM). Previously, ATLAS and CMS searches for DM were conducted within the context of both Effective Field Theories (EFTs) [1, 5, 32, 33] and full UV-complete theories such as Supersymmetry [10–12, 40]. The latter approach, though well-motivated, is typified by a broad parameter space and generally yields results which are insensitive to the wider class of DM models. EFT constraints, in comparison, are applicable to a broad range of models and rely on the specification of only a small set of parameters, namely the suppression scale,  $M_\star$ , and the DM mass,  $m_{\text{DM}}$  [25]. In the EFT framework, interactions between the dark and Standard Model (SM) sector are parametrised by a set of higher-dimensional effective operators, that arise when the mass of the mediating particle is assumed to be significantly larger than the momentum transferred in a given interaction. Where this is not the case, the EFT prescription can produce constraints which detour dramatically from those of the associated UV-complete model [24–28]. This is not so important in direct detection experiments where the momentum transferred in the scattering of DM particles with heavy nuclei is generally of the order of tens of MeV [13, 14], or in indirect searches where the annihilations of non-relativistic DM particles in the galactic halo occur with momentum transfers of order  $m_{\text{DM}}$ . However, for hadron collider searches - where the accessible center of mass energy of two colliding baryons may be sufficient to produce the mediator on-shell - the range of validity of the EFT prescription is significantly diminished. Indeed, recent works have shown the EFT approach to be problematic in certain cases for the interpretation of data collected during the  $\sqrt{s} = 8$  TeV Run I of the Large Hadron Collider (LHC) [15–17]. In light of this, simplified models have become the preferred tool for the interpretation of collider DM searches [18, 31, 53, 55, 56].

In a nutshell, a simplified model (SiM) arises when the heavy mediator which was integrated out in the EFT framework is reintroduced. Like EFTs, SiMs admit the comparison of results obtained in the different avenues of dark matter study [72, 73] and are defined by a relatively small set of parameters - namely  $m_{\text{DM}}$ , the mass of the mediator  $M_{\text{med}}$ , and the SM-mediator and DM-mediator coupling strengths,  $g_q$  and  $g_\chi$  (or  $g_{q\chi}$  in the case of a single, SM-DM-mediator coupling). Unlike EFTs, constraints calculated within the context of a SiM are valid across a broad energy range.

In this paper, we examine a phenomenologically distinct set of SiMs. In particular, we place constraints on the SiMs corresponding to the simplest UV-completions of the D5 (vector) and D8 (axial-vector) effective operators in the  $s$ -channel<sup>1</sup>. We also include a case in which a scalar mediator is exchanged in the  $t$ -channel, motivated by its analog of squark exchange in Supersymmetry. In the heavy mediator limit, this model can be expressed as a combination of operators D5 to D8 via a Fierz transformation.

---

<sup>1</sup>The D5 and D8 operators form a nice starting point in the analysis of SiMs as they have been studied exhaustively in the past (see refs. [1, 4, 5, 7, 15–17, 32, 33] among others). This attention is motivated by the fact that collider limits for the D5 (D8) operator can be readily transformed into limits on spin-independent (spin-dependent) DM-nucleon scattering and vice versa.

88 The models are constrained using public results from mono- $X$  + missing transverse  
 89 energy ( $E_T^{\text{miss}}$ ) searches conducted by the ATLAS Collaboration. Specifically we focus on  
 90 searches where  $X$  is either a parton (manifesting in the detector as a narrow-radius jet), a  
 91 leptonically-decaying  $Z$  boson, or a hadronically-decaying  $W$  or  $Z$  boson (manifesting as a  
 92 large-radius jet). The purpose of this work is to strengthen existing SiM limits using the  
 93 full  $20.3 \text{ fb}^{-1}$  of Run I ATLAS data, and to explore an enhanced phase space with respect  
 94 to the mediator and DM masses and the relative strength of the couplings to the visible  
 95 and dark sectors. We choose to treat the mediator width as the minimal value naturally  
 96 arising, which is more realistic than a fixed width. We extend the study by providing  
 97 a cross-check and comparison of the performance of the three targeted collider detection  
 98 channels, and compare against relic density and direct detection constraints.

99 The remainder of the paper is organised as follows. Section 2 contains a compendium of  
 100 the SiMs chosen for analysis and the associated collider phenomenology. Section 3 outlines  
 101 the techniques used to recast mono- $X$  +  $E_T^{\text{miss}}$  limits on the visible cross-section for any  
 102 new physics process into constraints on SiMs, and specifically on the couplings  $g_q$  and  $g_\chi$ .  
 103 Lastly, our results are presented in section 4 along with a discussion of the implications of  
 104 this work. Appendices A and B include details of the limit setting and analysis validation  
 105 procedures.

## 106 2 Simplified Model Phenomenology

### 107 2.1 Model Descriptions

108 We begin with a short set of assumptions: that the DM particle,  $\chi$ , is a weakly interacting  
 109 Dirac fermion, that it is a singlet under the SM, and that it is the lightest stable new  
 110 particle. Additionally the new sector is assumed to couple only to the SM quarks; while  
 111 possible coupling to SM leptons e.g. [26] or gluons e.g. [59] has been studied elsewhere, it  
 112 is beyond the scope of this paper. The nature of the mediating particle then results from  
 113 these assumptions: in the  $s$ -channel it is chosen to be a vector particle which must also be  
 114 a SM singlet, denoted  $\xi$ , while in the  $t$ -channel it is a scalar particle which is necessarily  
 115 charged and coloured, and labelled  $\phi$ .

116 The  $s$ -channel models chosen for analysis are characterised by vector ( $sV$ ) or axial-  
 117 vector ( $sA$ ) couplings to both the dark and SM sectors. They are described by the following  
 118 interaction Lagrangians:

$$\mathcal{L}_{sV} \supset -\xi_\mu \left[ \sum_q g_q \bar{q} \gamma^\mu q - g_\chi \bar{\chi} \gamma^\mu \chi \right], \quad (2.1)$$

119

$$\mathcal{L}_{sA} \supset \xi_\mu \left[ \sum_q g_q \bar{q} \gamma^\mu \gamma_5 q - g_\chi \bar{\chi} \gamma^\mu \gamma_5 \chi \right], \quad (2.2)$$

120 where the sum is over all quarks. For the couplings  $g_q$  and  $g_\chi$  to remain within the  
 121 perturbative regime, they are required to satisfy  $g_q, g_\chi \leq 4\pi$ , though stronger perturbativity  
 122 requirements do exist [15].

The  $t$ -channel model (abbreviated  $tS$ ) is primarily motivated by analogy with a common aspect of Supersymmetric models: neutralino DM interacting with the SM sector via  $t$ -channel exchange of a squark [20]. Note that in this Supersymmetric scenario the DM particle is a Majorana fermion. The collider phenomenology of a SiM in which  $\chi$  is of Majorana type is kinematically identical to the corresponding Dirac case (requiring multiplication of the cross-section by a simple factor in order to compute limits) and so Majorana DM is not covered here<sup>2</sup>. The exception to this rule is the  $s$ -channel vector mediator model, which vanishes if  $\chi$  is a Majorana fermion [21].

In the  $tS$  model, the mediator is allowed to couple to either the left or right-handed quarks as an SU(2) doublet or singlet respectively. Since the LHC is insensitive to the chirality of the quarks, we assume for simplicity that  $\phi$  couples to the left-handed quarks only, and is itself an SU(2) doublet, allowing radiation of a  $W$  boson. To avoid different couplings to quarks of different generations, and to remain in step with the DM forum recommendations [53], we include three generations of mediator doublets  $\phi_i$ , with equal masses and couplings. The interaction Lagrangian for this model is then:

$$\mathcal{L}_{tS} \supset \sum_i g_{q\chi} \bar{Q}_i P_R \phi_i \chi + \text{h.c.}, \quad (2.3)$$

where the sum is over the three quark doublets,  $g_{q\chi}$  is the DM-quark coupling (equal for each generation), and  $P_R$  is the usual chiral projection operator.

## 2.2 The Mono- $X + E_T^{\text{miss}}$ Signature

The mono- $X + E_T^{\text{miss}}$  signal (abbreviated to mono- $X$ ) is a popular collider signal in the search for new physics, particularly in the search for dark matter. Since DM particles are not expected to interact with detector material, they appear as missing transverse energy when balanced against a visible object,  $X$ , that is radiated from the initial or intermediate state. For the  $s$ -channel SiMs discussed above, only initial-state radiation is permitted; see figs. 1a and 1b for examples. For the  $tS$  model, radiation of a gluon or electroweak (EW) boson is permitted both from initial state partons (fig. 1c) or from the mediator (fig. 1d).

The most likely scenario at the LHC is production of a jet alongside the invisible  $\chi$  pair, as a result of the strong coupling and prevalence of partons in the initial state. However, to fully exploit the potential of the ATLAS detector to record and identify a vast array of particle types, we also consider two additional channels. Firstly, we take advantage of the relative cleanliness and simplicity of leptons in the leptonically-decaying mono- $Z(\rightarrow \ell^+ \ell^-)$  channel. We also take advantage of the large hadronic branching fraction, and developing jet-identification techniques for boosted EW bosons, in the hadronically-decaying mono- $W/Z(\rightarrow jj)$  channel<sup>3</sup>. In both cases, the large multi-jet background is reduced, and complications in jet production such as parton-matching can be ignored, making these an interesting alternative to the mono-jet channel where speed, efficiency and a reduction in jet-associated uncertainties may make up for a loss in sensitivity.

<sup>2</sup>The exception being in the validation of the mono- $Z(\text{lep})$  channel, see Sec. B.2.

<sup>3</sup>In addition, one of the first Run II dark matter search results from ATLAS was from this channel [60], released during the preparation of this paper.

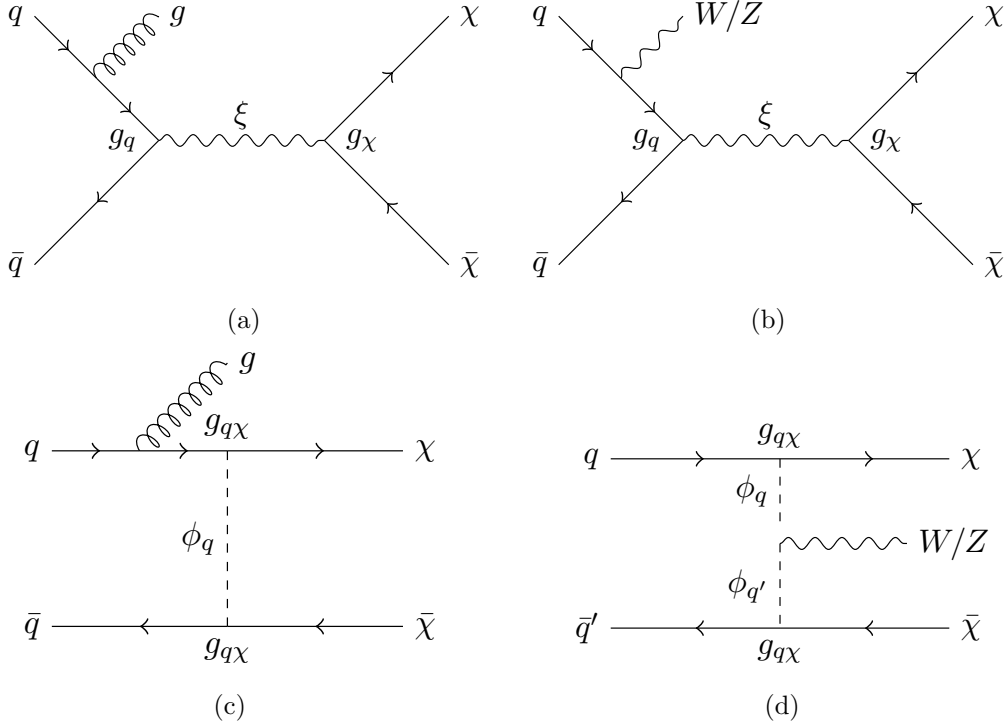


**Figure 1:** Representative dark matter pair-production processes with a gluon or  $W/Z$  boson in the final state for the  $s$ -channel (a,b) and  $t$ -channel (c,d) models.

### 2.3 Mass and Coupling Points

A representative set of dark matter and mediator masses, listed in table 1, are chosen for study in each detection channel. DM masses of 3, 30 and 300 GeV are also included in the mono- $Z$ (lep) channel, where ease of production permits higher granularity. All  $(m_\chi, M_{\text{med}})$  combinations are allowed in the  $sV$  and  $sA$  models, while in the  $tS$  model  $M_{\text{med}}$  must be greater than  $m_\chi$  to ensure stability of the DM particle. The couplings  $g_q$  and  $g_{q\chi}$  are set to unity, while the DM-mediator coupling in the  $s$ -channel models,  $g_\chi$ , is varied from 0.2 to 5. The mediator masses are chosen to cover a broad range of parameter space and to coincide with predominantly three regimes: (near-)degenerate ( $M_{\text{med}} \approx m_\chi$ ), on-shell ( $M_{\text{med}} \geq 2m_\chi$ ) and off-shell ( $M_{\text{med}} < 2m_\chi$ ).

### 2.4 Treatment of the width

An important factor when considering SiMs is to ensure that the mediator width is treated appropriately, as it impacts both the cross-section calculation and, in some cases, the kinematic behaviour of the model.

Following the DM Forum recommendations [53], we use the minimal width, allowing coupling to all kinematically accessible quarks. We assume minimal flavour violation, which implies a universal coupling to all quark flavours. The minimum width for each model is given by:

$m_\chi$ [GeV]	$M_{\text{med}}$ [GeV]	s-channel		t-channel
		$g_q$	$g_\chi$	$g_{q\chi}$
1, (3), 10, (30), 100, (300), 1000	1, 2, 10, 20, 100, 200, 1000, 2000	1	0.2, 0.5, 1, 2, 5	1

**Table 1:** Mass and coupling points chosen for the analysis of simplified dark matter models. Values in brackets are only included in the mono- $Z(\text{lep})$  channel. The mediator masses are primarily representative of three regimes: (near-)degenerate ( $M_{\text{med}} \approx m_\chi$ ), on-shell ( $M_{\text{med}} \geq 2m_\chi$ ) and off-shell ( $M_{\text{med}} < 2m_\chi$ ). For the  $t$ -channel model,  $M_{\text{med}} > m_\chi$  is required to ensure stability of the DM particle.

$$\begin{aligned} \Gamma_{sV} = & \frac{g_\chi^2 M}{12\pi} \left(1 + \frac{2m_\chi^2}{M^2}\right) \left(1 - \frac{4m_\chi^2}{M^2}\right)^{\frac{1}{2}} \Theta(M - 2m_\chi) \\ & + \sum_q \frac{g_q^2 M}{4\pi} \left(1 + \frac{2m_q^2}{M^2}\right) \left(1 - \frac{4m_q^2}{M^2}\right)^{\frac{1}{2}} \Theta(M - 2m_q) \end{aligned} \quad (2.4)$$

$$\begin{aligned} \Gamma_{sA} = & \frac{g_\chi^2 M}{12\pi} \left(1 - \frac{4m_\chi^2}{M^2}\right)^{\frac{3}{2}} \Theta(M - 2m_\chi) \\ & + \sum_q \frac{g_q^2 M}{4\pi} \left(1 - \frac{4m_q^2}{M^2}\right)^{\frac{3}{2}} \Theta(M - 2m_q) \end{aligned} \quad (2.5)$$

$$\begin{aligned} \Gamma_{tS} = & \sum_q \frac{g_{q\chi}^2 M}{16\pi} \left(1 - \frac{m_q^2}{M^2} - \frac{m_\chi^2}{M^2}\right) \\ & \times \sqrt{\left(1 - \frac{m_q^2}{M^2} + \frac{m_\chi^2}{M^2}\right)^2 - 4\frac{m_\chi^2}{M^2}} \Theta(M - m_q - m_\chi) \end{aligned} \quad (2.6)$$

177 It is possible that the mediator may decay to other SM or BSM particles [31], but this  
178 is not expected to have a large effect on the kinematic distribution as long as the width  
179 remains relatively small [53]. The generator treatment of the mediator as a Breit-Wigner  
180 propagator, rather than a true kinetic propagator, breaks down for large widths [57, 70].

181 We can take advantage of the fact that for each point in  $(m_\chi, M_{\text{med}})$  phase space,  
182 the mediator width (and therefore the couplings) do not greatly affect a model's kinematic  
183 behaviour (with the notable exception of the  $tS$  model in the mono-jet channel). This is  
184 demonstrated in fig. 2, where we plot a simplified  $E_T^{\text{miss}}$  distribution (as a proxy for the full  
185 selection in each analysis) for the  $sV$  (representing both the  $sV$  and  $sA$  models) and  $tS$   
186 models for two mass points and a demonstrative set of couplings such that  $\Gamma < M_{\text{med}}/2$ .  
187 The  $E_T^{\text{miss}}$  distribution is predominantly independent of the mediator width for the  $s$ -  
188 channel models in the mono-jet channel, and all models in the mono- $Z(\text{lep})$ <sup>4</sup> channel.

<sup>4</sup>In this discussion, the mono- $W/Z(\text{had})$  channel can be assumed to follow the same logic as for the

189 However, there is a clear variation in the kinematic behaviour of the  $tS$  model in the mono-  
 190 jet channel, which can be attributed to additional diagrams (accessible only in this channel)  
 191 featuring a gluon in the initial state and subsequently allowing the mediator to go on-shell.  
 192 In this scenario, when the resulting quark and DM particle are both small compared to the  
 193 mediator mass, they share equally its energy leading to a peak in the  $E_T^{\text{miss}}$  distribution at  
 194 approximately half the mediator mass.

195 In the cases where the kinematic distribution is independent of the width, we assume  
 196 that the impact of the selection cuts in each channel is unchanged by the couplings. In  
 197 this case, the following relations approximately hold:

$$\sigma \propto \begin{cases} g_q^2 g_\chi^2 / \Gamma & \text{if } M_{\text{med}} \geq 2m_{\text{DM}} \\ g_q^2 g_\chi^2 & \text{if } M_{\text{med}} < 2m_{\text{DM}} \end{cases} \quad (2.7)$$

198 in the  $sV$  and  $sA$  models [57], and

$$\sigma \propto g_{q\chi}^4 \quad (2.8)$$

199 in the  $tS$  model. When valid, these approximations allow us to greatly simplify our limit  
 200 calculations, and for this reason, we restrict our primary results to regions of parameter  
 201 space where  $\Gamma/M < 0.5$ . See app. A for further details of the limit-setting calculation.

202 More problematically, it was noted by refs. [57, 70] that the Breit-Wigner propagator  
 203 breaks down in the  $m_{\text{DM}} \gg M_{\text{med}}$  region even if  $\Gamma/M$  is small. To correct for this we follow  
 204 ref. [57], and rescale the cross section in the  $m_{\text{DM}} > M_{\text{med}}$  region by a factor which takes into  
 205 account the error introduced by using the Breit-Wigner propagator in the generator. The  
 206 factor is found by convolving the PDF with both the kinetic and Breit-Wigner propagators  
 207 in turn and taking the ratio at each mass point. We approximate the kinetic propagator  
 208 by making the substitution  $M\Gamma(M) \rightarrow s\Gamma(\sqrt{s})/M$  in the Breit-Wigner propagator.

209 A full study of the  $tS$  model within the mono-jet channel, where altering the coupling  
 210 can lead to changed kinematic behaviour, has been performed elsewhere [23], and requires  
 211 the production of individual samples for each coupling point. This, combined with the  
 212 challenges associated with including differing orders of  $\alpha_s$ , make the generation process  
 213 computationally expensive compared to the mono- $Z(\text{lep})$  and mono- $W/Z(\text{had})$  channels.  
 214 We therefore exclude an analysis of the  $tS$  model in the mono-jet channel in this work.

### 215 3 Recasting mono- $X$ constraints

216 The procedure for recasting existing mono- $X$  analyses to obtain SiM constraints follows a  
 217 simple cut-and-count methodology. Firstly, signal events are simulated (described below  
 218 in section 3.1) with object  $p_T$  smearing applied to approximate the detection efficiency of  
 219 the ATLAS detector,  $\epsilon$ . The event selection criteria of the mono- $X$  analysis of interest  
 220 is then applied to the simulated signal samples. Events surviving the selection criteria  
 221 are counted to determine the likelihood of a dark matter event being observed (referred

---

mono- $Z(\text{lep})$  channel.





**Figure 2:** The  $E_T^{\text{miss}}$  distribution of the  $sV$  and  $tS$  models in the mono-jet and mono- $Z(\text{lep})$  channels, for some demonstrative masses. The parameter  $\mu$  is defined as  $\Gamma/M_{\text{med}}$ , and is used to demonstrate the impact of a changing width; in particular, the  $tS$  model in the mono-jet channel shows clear width-dependence. The widths are obtained with couplings of 0.1, 1, and 5 where  $\mu < 0.5$  remains true.

to as the acceptance,  $\mathcal{A}$ ), which is then used in combination with channel-specific model-independent limits on new physics events to limit the parameter phase space of a given model. For a comprehensive description of the recasting procedure, see appendix A.

In this paper, mono-jet constraints are derived from a search for new phenomena conducted by the ATLAS Collaboration using  $pp$  collisions at  $\sqrt{s} = 8$  TeV as described in ref. [41]. Similarly, the leptonic mono- $Z$  and hadronic mono- $W/Z$  constraints are derived from ATLAS dark matter searches that were optimised for the D1, D5 and D9 effective operators [47, 48]. These analyses are described in further detail in sections 3.2, 3.3 and 3.4 respectively.

### 3.1 Signal Simulation

Monte Carlo simulated event samples are used to model the expected signal for each channel and for each SiM. Leading order matrix elements for the process  $pp \rightarrow X + \chi\bar{\chi}$  (where

<sup>234</sup>  $X$  is specifically one or two jets<sup>5</sup>, a  $Z(\rightarrow \ell^+\ell^-)$  boson or a  $W/Z(\rightarrow jj)$  boson) are first  
<sup>235</sup> simulated using MADGRAPH5\_aMC@NLO v2.2.2 [49] with the MSTW2008lo68cl PDF [50].  
<sup>236</sup> During this stage, the renormalisation and factorisation scales are set to the default sum  
<sup>237</sup> of  $\sqrt{m^2 + p_T^2}$  for all particles in the final state. Showering and hadronisation are then  
<sup>238</sup> performed by PYTHIA 8 .201 [58] with the appropriate PDF and using the ATLAS UE  
<sup>239</sup> Tune AU2-MSTW2008LO [51]. Reconstruction of small-radius jets (hereon referred to  
<sup>240</sup> just as ‘jets’) for the mono-jet channel is performed by FASTJET [63] using the anti- $k_T$   
<sup>241</sup> algorithm with radius parameter  $R = 0.4$ . Similarly, reconstruction of large-radius jets for  
<sup>242</sup> the mono- $W/Z(\text{had})$  channel is performed using the Cambridge-Aachen algorithm with  $R$   
<sup>243</sup>  $= 1.2$ . The latter channel also includes a mass-drop filtering procedure with  $\mu = 0.67$  and  
<sup>244</sup>  $\sqrt{y}^6 = 0.4$  (see ref. [62] for further details), which favours large- $R$  jets with two balanced  
<sup>245</sup> subjets, consistent with the decay of an EW boson to a (potentially-boosted) dijet pair.  
<sup>246</sup> Lastly, the detector response is approximated by applying a Gaussian smearing factor to  
<sup>247</sup> the  $p_T$  of all leptons and jets.

### <sup>248</sup> 3.1.1 Parton Matching Scheme

<sup>249</sup> In the ATLAS mono-jet analysis, matching of partons generated in MADGRAPH5 to jets  
<sup>250</sup> generated in PYTHIA 8 is performed using the MLM scheme [61], with two matching scales,  
<sup>251</sup> or values of ‘QCUT’, per mass/coupling point. In combination, the QCUT values span a  
<sup>252</sup> broad kinematic range with a cut placed on the leading jet  $p_T$  per event to avoid double-  
<sup>253</sup> counting. This treatment aims to mitigate the impact of the matching scale on the shape  
<sup>254</sup> of the  $p_T$  and  $E_T^{\text{miss}}$  distributions; that is, to reduce the uncertainty in those areas of phase  
<sup>255</sup> space where the transferred momentum is significantly larger or smaller than the QCUT  
<sup>256</sup> value. For the analysis of SiMs, we use instead a single matching scale of 80 GeV. Though  
<sup>257</sup> not ideal, this approach suitably reproduces the results of the ATLAS mono-jet analysis  
<sup>258</sup> for the masses of interest (see Sec. B.1). Importantly, it also reduces the complexity and  
<sup>259</sup> computational expense involved in estimating limits for the mono-jet channel.

<sup>260</sup> We now move to a discussion of each of the mono- $X$  channels separately.

## <sup>261</sup> 3.2 Mono-jet Constraints

<sup>262</sup> The ATLAS mono-jet +  $E_T^{\text{miss}}$  analysis [41] was originally designed to set limits on three  
<sup>263</sup> new physics scenarios, the most relevant of which is the production of WIMP DM within  
<sup>264</sup> the context of a set of effective operators. The analysis also includes a brief study of a  $Z'$   
<sup>265</sup> DM model which is analogous to our  $sV$  model.

<sup>266</sup> Signal selection is carried out based on at least one hard jet recoiling against missing  
<sup>267</sup> energy. To ensure that the correct back-to-back jet +  $E_T^{\text{miss}}$  topology is selected events are  
<sup>268</sup> required to have a leading jet,  $j_1$ , with  $p_T > 120$  GeV and  $|\eta| < 2.0$  satisfying  $p_T^{j_1}/E_T^{\text{miss}} >$   
<sup>269</sup>  $0.5$ . Surviving events must then satisfy  $|\Delta\phi(j, \vec{E}_T^{\text{miss}})| > 1.0$ , where  $j$  is any jet with  $p_T >$   
<sup>270</sup>  $30$  GeV and  $|\eta| < 4.5$ . This criterion reduces the multijet background contribution where  
<sup>271</sup> the large  $E_T^{\text{miss}}$  originates mainly from jet energy mismeasurement. Note that there is no

<sup>5</sup>Jets are seeded by any parton excluding the (anti-)top quark.

<sup>6</sup> $\sqrt{y} = \min(p_{T_{j_1}}, p_{T_{j_2}})\Delta R/m_{jet}$  is the momentum balance of the two leading subjets.

upper limit placed on the number of jets per event. The contribution from the dominant background processes,  $W/Z$ +jets, is managed with a veto on events containing muons or electrons with  $p_T > 7$  GeV. Lastly, nine separate signal regions are defined with increasing lower thresholds on  $E_T^{\text{miss}}$ , which range from 150 GeV to 700 GeV as shown in table 2.

The ATLAS mono-jet analysis revealed no significant deviation of observed events from the expected SM backgrounds in the Run 1 8 TeV dataset. Subsequently, model-independent limits on new physics signatures were provided in terms of the visible cross-section,  $\sigma \times \mathcal{A} \times \epsilon$ ; these are listed in table 2.

Signal Region	$E_T^{\text{miss}}$ threshold [GeV]	$\sigma \times \mathcal{A} \times \epsilon$ [fb]
SR1	150	726 (935)
SR2	200	194 (271)
SR3	250	90 (106)
SR4	300	45 (51)
SR5	350	21 (29)
SR6	400	12 (17)
SR7	500	7.2 (7.2)
SR8	600	3.8 (3.2)
SR9	700	3.4 (1.8)

**Table 2:** The ATLAS mono-jet  $E_T^{\text{miss}}$  signal regions and corresponding observed (expected) model-independent upper limits on  $\sigma \times \mathcal{A} \times \epsilon$  at 95% confidence level. Adapted from ref. [41].

The signal simulation procedure outlined in sec. 3.1 and implementation of the selection criteria discussed above were validated for the mono-jet channel via reproduction of ATLAS limits on the suppression scale,  $M_\star \equiv M_{\text{med}}/\sqrt{g_q g_\chi}$ , for the  $Z'$  model. The details of this process are contained in appendix B.1. Importantly, we observe agreement within  $\sim 12\%$  for all samples.

### 3.3 Mono- $Z(\text{lep})$ Constraints

The ATLAS mono- $Z(\rightarrow \ell^+ \ell^-) + E_T^{\text{miss}}$  analysis [47] was principally designed to constrain a set of EFT models of DM. As a secondary focus, it also includes a short study of a  $t$ -channel SiM similar to our  $tS$  model.

The selection criteria for this analysis are summarised as follows (see the paper for a full description). Electrons (muons) are required to have a  $p_T$  greater than 20 GeV, and  $|\eta|$  less than 2.47 (2.5). Two opposite-sign, same-flavour leptons are selected, and required to have invariant mass and pseudorapidity such that  $m_{\ell\ell} \in [76, 106]$  GeV and  $|\eta^{\ell\ell}| < 2.5$ . The reconstructed  $Z$  boson should be approximately back-to-back and balanced against the  $E_T^{\text{miss}}$ , ensured with the selections  $\Delta\phi(\vec{E}_T^{\text{miss}}, p_T^{\ell\ell}) > 2.5$  and  $|p_T^{\ell\ell} - E_T^{\text{miss}}|/p_T^{\ell\ell} < 0.5$ . Events containing a jet with  $p_T > 25$  GeV and  $|\eta| < 2.5$  are vetoed. Events are also vetoed if they contain a third lepton with  $p_T > 7$  GeV. The signal regions are defined by increasing lower  $E_T^{\text{miss}}$  thresholds:  $E_T^{\text{miss}} > 150, 250, 350, 450$  GeV.

298 A cut-and-count strategy is used to estimate the total observed yields and expected SM  
 299 backgrounds in each signal region. The limits on  $\sigma \times \mathcal{A} \times \epsilon$  are not publicly available, so we  
 300 take the numbers of expected and observed events, along with the associated uncertainties,  
 301 and convert these into model-dependent upper limits with a single implementation of the  
 302 HistFitter framework [54] using a frequentist calculator and a one-sided profile likelihood  
 303 test statistic (the LHC default). The results of this process are displayed in table 3. Note  
 304 that we use signal regions 1 and 2 only, as our simplified HistFitter approach is inadequate  
 305 to handle the very low statistics of signal regions 3 and 4. These upper limits are also  
 306 used for the validation of the mono- $Z(\text{lep})$  signal generation and selection procedures (see  
 307 app. B.2).

Signal Region	$E_{\text{T}}^{\text{miss}}$ threshold [GeV]	$\sigma \times \mathcal{A} \times \epsilon$ [fb]
SR1	150	1.59 (1.71)
SR2	250	0.291 (0.335)

**Table 3:** The ATLAS mono- $Z(\text{lep})$   $E_{\text{T}}^{\text{miss}}$  signal regions and corresponding observed (ex-  
 pected) model-independent upper limits on  $\sigma \times \mathcal{A} \times \epsilon$  at 95% confidence level. Adapted  
 using HistFitter from ref. [47].

### 308 3.4 Mono- $W/Z(\text{had})$ Constraints

309 The ATLAS mono- $W/Z(\text{had}) + E_{\text{T}}^{\text{miss}}$  search [48] was aimed at constraining the spin-  
 310 independent effective operators C1, D1, and D5, and the spin-dependent operator D9. The  
 311 search was originally designed to exploit the constructive interference of  $W$  boson emission  
 312 from opposite-sign up-type and down-type quarks, leading to DM production wherein the  
 313 mono- $W$  channel is dominant. Recent studies [64] have revealed this scenario to violate  
 314 gauge invariance and so we ignore it in this analysis.

315 The mono- $W/Z(\text{had})$  event selection is carried out as follows. Large-radius jets are  
 316 selected using a mass-drop filtering procedure (see sec. 3.1) to suppress non- $W/Z$  processes.  
 317 Events are required to contain at least one large- $R$  jet with  $p_{\text{T}} > 250$  GeV,  $|\eta| < 1.2$  and  
 318 a mass,  $m_{\text{jet}}$ , within a 30-40 GeV window of the  $W/Z$  mass (i.e.  $m_{\text{jet}} \in [50, 120]$  GeV).  
 319 In order to reduce the  $t\bar{t}$  and multijet backgrounds, a veto removes events containing a  
 320 small- $R$  jet with  $\Delta\phi(\text{jet}, E_{\text{T}}^{\text{miss}}) < 0.4$ , or containing more than one small- $R$  jet with  $p_{\text{T}} >$   
 321 40 GeV,  $|\eta| < 4.5$ , and  $\Delta R(\text{small-}R \text{ jet, large-}R \text{ jet}) > 0.9$ . Electrons, muons and photons  
 322 are vetoed if their  $p_{\text{T}}$  is larger than 10 GeV and they lie within  $|\eta| < 2.47$  (electrons),  
 323 2.5 (muons), 2.37 (photons). Two signal regions were defined with  $E_{\text{T}}^{\text{miss}} > 350$  GeV and  
 324  $E_{\text{T}}^{\text{miss}} > 500$  GeV.

325 The ATLAS analysis used a shape-fit of the mass distribution of the large- $R$  jet to  
 326 estimate the background yields in the two signal regions, along with the associated statis-  
 327 tical and systematic uncertainties. As in the mono- $Z(\text{lep})$  case, we do not take the shapes  
 328 into account but convert the published number of expected and observed events into upper  
 329 limits on the expected and observed number of new physics events using the HistFitter

framework. For the  $E_T^{\text{miss}} > 500$  GeV signal region, we obtain the limits shown in table 4. We do not consider the first signal region with  $E_T^{\text{miss}} > 350$  GeV in the recasting procedure, since the cut-and-count limits extracted could not be convincingly validated. The high  $E_T^{\text{miss}}$  signal region was found to be optimal for most operators studied by the ATLAS analysis.

Signal Region	$E_T^{\text{miss}}$ threshold [GeV]	$\sigma \times \mathcal{A} \times \epsilon$ [fb]
SR2	500	1.35 (1.34)

**Table 4:** The ATLAS mono- $W/Z(\text{had})$   $E_T^{\text{miss}}$  signal region considered in this work and corresponding observed (expected) model-independent upper limits on  $\sigma \times \mathcal{A} \times \epsilon$  at 95% confidence level. Adapted using HistFitter from ref. [48].

## 4 Results and Discussion

### 4.1 Limits on the coupling $\sqrt{g_q g_\chi}$

The 95% confidence level upper limits on the  $sV$  and  $sA$  model coupling combination  $\sqrt{g_q g_\chi}$ , and the  $tS$  model coupling  $g_{q\chi}$ , obtained from each of the mono- $X$  channels, are presented in figs. 3-8. These quantities were evaluated as described in appendix A (including statistical and systematic uncertainties), and correspond to the best limits of each signal region tested.

In each plot, limits are shown ranging from  $<0.01$  to the upper perturbative limit<sup>7</sup> for each coupling,  $4\pi$ ; where a limit was calculated to be larger than this, the limit is considered meaningless and the region is coloured grey. The white (hatched) regions coincide with those mass points which yield an initial (final) value of  $\sqrt{g_q g_\chi}$  or  $g_{q\chi}$  which fails to satisfy  $\Gamma < M_{\text{med}}/2$ . (We observe that values for which the width is just within our upper validity bound of  $M_{\text{med}}/2$  may be pushed over into the invalid range with the addition of new particles, not considered here, which would serve to increase the mediator width.) When  $g_\chi/g_q = 0.2$ , only the mono-jet channel produces limits which survive this requirement, and so these are shown separately in fig 7.

Detailed comments specific to each channel are provided below, however some trends are channel-independent. For the  $sV$  model, strong limits exist when  $M_{\text{med}} > 2m_\chi$  as the mediator can go on-shell, thereby enhancing the cross-section. The  $sA$  model limits are generally similar to the  $sV$  model limits except in the region corresponding to  $m_{\text{DM}} \gtrsim \sqrt{4\pi} M_{\text{med}}/g_\chi^{\text{gen}}$  where  $g_\chi^{\text{gen}}$  is the DM coupling used at the generator level. We remove this region in the  $sA$  model to avoid violating perturbative unitarity, which can lead to an unphysical enhancement of the cross-section when the DM mass is much larger than the mediator mass [71]. The upper limit on  $\sqrt{g_q g_\chi}$  is relatively constant across values of  $g_\chi/g_q$ , as is expected when the coupling (and hence the width) has been demonstrated to have

<sup>7</sup>We note that perturbativity is questionable for couplings greater than  $\sim 2 - 3$ , however  $4\pi$  is an oft-quoted hard upper limit.

little effect on kinematic behaviour (see sec 2.4), and using the assumptions of eq. 2.7. As the ratio increases, points in the region  $M_{\text{med}} > m_\chi$  disappear as the initial value,  $g_q = 1$ , leads to a failure of the width condition. However, one could easily chose a smaller initial value of  $g_q$  to recover these points, and we suggest that the limits in this region would be quite similar to those seen in the  $g_\chi/g_q = 0.2$  and 0.5 cases.

The constraints on the coupling strength are weaker when  $m_\chi$  or  $M_{\text{med}}$  is large ( $>100$  GeV) owing to suppression of the cross-section. In this region, the constraints are expected to improve at higher centre-of-mass energies. For small DM masses with an off-shell mediator, the  $E_{\text{T}}^{\text{miss}}$  distribution is softer, therefore results in this region of phase space are limited by statistical uncertainties associated with the tail-end of the distribution. This region of phase space would benefit from further optimisation of event selection in analyses aimed at the study of simplified models, as we expect to see in the upcoming Run II results.

These mono- $X$  searches are complementary to direct searches for the mediator via dijet resonances [29, 67–69]. These have been used to study SiMs in, for example, [23, 70]. Dijet studies search for the signature of direct mediator decay into standard model particles, generally assuming a narrow resonance. These constraints can be stronger than mono- $X$  constraints particularly when the width is small and when the coupling to quarks is large relative to the coupling to DM. Mono- $X$  searches however have the advantage for larger values of  $g_\chi/g_q$  and smaller mediator masses.

We now examine channel-specific trends.

#### 4.1.1 Mono-jet channel

The mono-jet channel upper limits on the coupling combination  $\sqrt{g_q g_\chi}$  for the  $sV$  and  $sA$  models are displayed in the left-hand column of figs. 3-6, for  $g_\chi/g_q = 0.5, 1, 2$  and 5 respectively (where the ratio of 5 is only shown for the  $sV$  model, due to a lack of meaningful results in the  $sA$  model). The  $g_\chi/g_q = 0.2$  case is shown separately in fig. 7, as these limits are only meaningful within this channel.

As expected, the mono-jet channel produces the strongest coupling limits for both  $s$ -channel models, which are better than those from the next-best mono- $Z(\text{lep})$  channel by a factor of a few. For these models, the weakest limits result for large  $m_\chi$  or large  $M_{\text{med}}$ , and in fact are so weak that they are pushed into the region of invalidity where  $\Gamma > M_{\text{med}}/2$ . Although the acceptance is considerably higher when both  $m_{\text{DM}}$  and  $M_{\text{med}}$  are large compared to low masses, the cross-section is sufficiently small so as to nullify any gain. Within the valid region ( $m_\chi \in [1, 100]$  GeV and  $M_{\text{med}} \in [1, 200]$  GeV), the limit on  $\sqrt{g_q g_\chi}$  generally ranges from 0.1 to 0.7, with a handful of on-shell masses reaching a limit of  $\sim 0.05$  in the large  $g_\chi/g_q$  case. In the large  $g_\chi/g_q$  scenario, limits for  $m_\chi = 1000$  GeV start to become valid; where  $\sqrt{g_q g_\chi}$  remains constant but  $g_\chi/g_q$  increases, the value of  $g_q$  is pushed downward and so the width, which is dominated by decays to SM particles, decreases with respect to  $m_{\text{DM}}$ .

The uncertainties on the limits for both  $s$ -channel models are dominated by contributions from the matching scale at acceptance-level, and generally range from  $\sim 5\%$  to 46%.

### 401 4.1.2 Mono- $Z(\text{lep})$ channel

402 The simplicity of the mono- $Z(\text{lep})$  channel relative to the mono-jet channel, and the ease  
 403 of signal simulation at MADGRAPH5 level allowed us to study a finer granularity of points  
 404 in the mass phase space. The resulting limits on the  $sV$  and  $sA$  models are shown in the  
 405 central column of figs. 3-6. While the behaviour of the limits as  $g_\chi/g_q$  is varied is similar  
 406 to that within the mono-jet channel, the mono- $Z(\text{lep})$  limits are overall weaker by a factor  
 407 of a few.

408 The total relative uncertainties on  $\sqrt{g_q g_\chi}$  for the  $s$ -channel models are generally within  
 409 10%, but can range up to 80% in a few cases where  $m_\chi$  is small; they are in general split  
 410 equally between statistical and systematic contributions.

411 The advantage of the mono-boson channels is in the study of the  $tS$  model; since this  
 412 was not included in the mono-jet channel the strongest limits are obtained with the mono-  
 413  $Z(\text{lep})$  analysis, and are shown in the left-hand side of fig. 8. Note that, in comparison to  
 414 the  $s$ -channel models, the limits have weakened by a factor of 10. This is the result of an  
 415 orders-of-magnitude weaker cross-section and the inability of the mediator to go on-shell  
 416 in this channel. We find stronger limits for smaller  $m_\chi$  and  $M_{\text{med}}$  masses, where larger  
 417 cross-sections compensate for lower acceptances at these points. Overall the uncertainties  
 418 contribute less than 10%.

### 419 4.1.3 Mono- $W/Z(\text{had})$ channel

420 The limits on the couplings of the  $sV$ ,  $sA$  and  $tS$  models, obtained within the mono-  
 421  $W/Z(\text{had})$  channel, are shown in the right-hand column of figs. 3-8. This channel was  
 422 included for comparison with the leptonic mono- $Z(\text{lep})$  channel in particular, but a coarser  
 423 selection of masses was chosen as the limits were initially found to be somewhat weaker.  
 424 Additionally, further estimates were made: a) as the kinematic behaviour is reasonable in-  
 425 dependent of the couplings, a single acceptance was found for each  $(m_\chi, M_{\text{med}})$  combination  
 426 and applied to each value of  $g_\chi/g_q$ , and b) complete systematic uncertainties were gener-  
 427 ated for a subset of masses and compared to those from the mono- $Z(\text{lep})$  channel; from  
 428 this comparison the mono- $Z(\text{lep})$  systematic uncertainties were multiplied by 2.3 and then  
 429 applied to the mono- $W/Z(\text{had})$  limits. As a result, the limits obtained in this channel are  
 430 not intended to be rigorously quantitative; rather, they are used to indicate qualitatively  
 431 how the channel compares.

432 The ATLAS mono- $W/Z(\text{had})$  analysis (and in particular the higher  $E_{\text{T}}^{\text{miss}}$  signal re-  
 433 gion) was not optimised for a SiM interpretation, and much of the phase space produced  
 434 insignificant numbers of events passing the event selection, with up to 200 thousand events  
 435 generated. Generally, the limits are a factor of a few weaker than those from the mono-  
 436  $Z(\text{lep})$  channel, which is both consistent with the limits on the EFT models studied in the  
 437 ATLAS analyses, and expected following our use of a cut-and-count interpretation, rather  
 438 than a shape analysis, of the mono- $W/Z(\text{had})$  public results.

439 In some cases the limits become comparable with the mono- $Z(\text{lep})$  channel, suggesting  
 440 that more statistics and an improved treatment of systematic uncertainties would bring  
 441 these closer in line with that channel.



Overall, the uncertainties from this channel lie within 5 to 50%, most of the time being between 10 and 30%. Generally, both statistical and systematic uncertainties contribute in a similar manner. A few points are clearly limited by the generated statistics, resulting in a statistical error of up to 90%. Points with high  $m_\chi$  and low  $M_{\text{med}}$  tend to have larger systematic uncertainties.

## 4.2 Comparison with Relic Density Constraints

In figs. 3-8 we show lines where the constraint on the coupling corresponds to the coupling strength that would reproduce the correct DM relic density if DM is a thermal relic of the early universe. For points diagonally above and to the left of the purple dashed line, the LHC constraints naively rule out the couplings leading to the correct relic density. Below and to the right of this line the relic density coupling is still allowed. In some cases the intercept does not pass through a significant number of data points surviving the quality criteria outlined in previous sections. In these cases the line is not shown.

In this scenario, the measured abundance is approximately related to the unknown self-annihilation cross-section via:

$$\Omega_{\text{DM}} h^2 \simeq \frac{2 \times 2.4 \times 10^{-10} \text{ GeV}^{-2}}{\langle \sigma v \rangle_{\text{ann}}}. \quad (4.1)$$

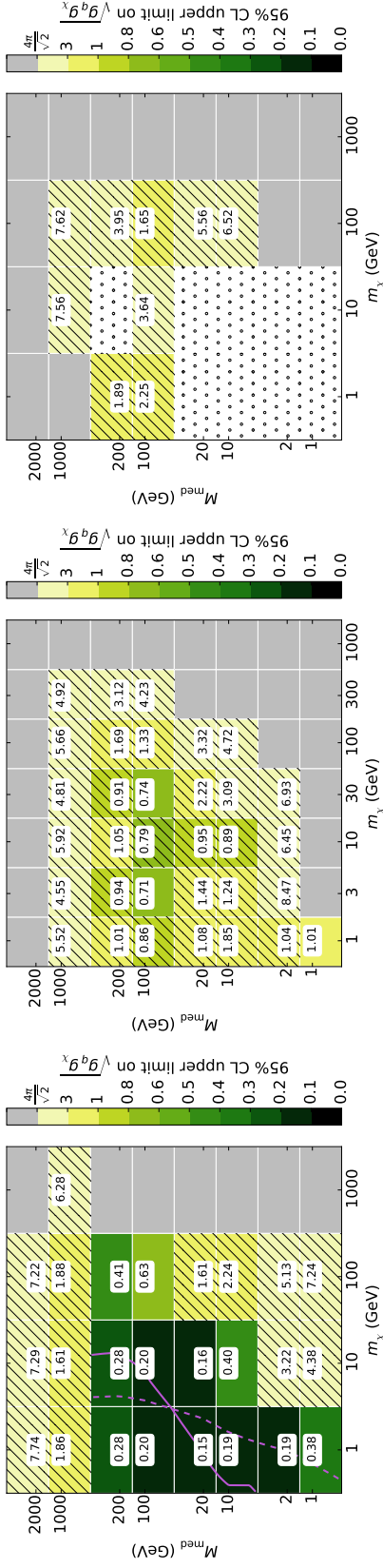
This is used with measurements of the DM abundance by Planck,  $\Omega_{\text{DM}}^{\text{obs}} h^2 = 0.1199 \pm 0.0027$  [36], to find  $\langle \sigma v \rangle_{\text{ann}} \simeq 4.0 \times 10^{-9} \text{ GeV}^{-2}$  for thermal relic DM. This relation is only approximately accurate, and so we use the micrOMEGAs code [52] to determine the coupling strength leading to the correct relic density for each model. This technique was verified against the semi-analytic technique outlined in e.g. ref. [37].

If the DM mass lies at the electroweak scale, the thermal relic scenario provides a natural explanation for the observed DM density. The coupling strengths leading to the correct relic density are therefore a natural benchmark with which to compare constraints from collider (and indeed direct detection) searches. However the relic density couplings should by no means be regarded as serious constraints. If DM is not produced thermally or there is an unknown effect which modifies the evolution of the density with temperature, then eq 4.1 breaks down. Additionally, in the scenario where we assume DM to be a thermal relic, we ignore the possibility of there being other annihilation channels and other beyond-SM particles contributing to the DM abundance, which, if taken into account, would also invalidate eq 4.1.

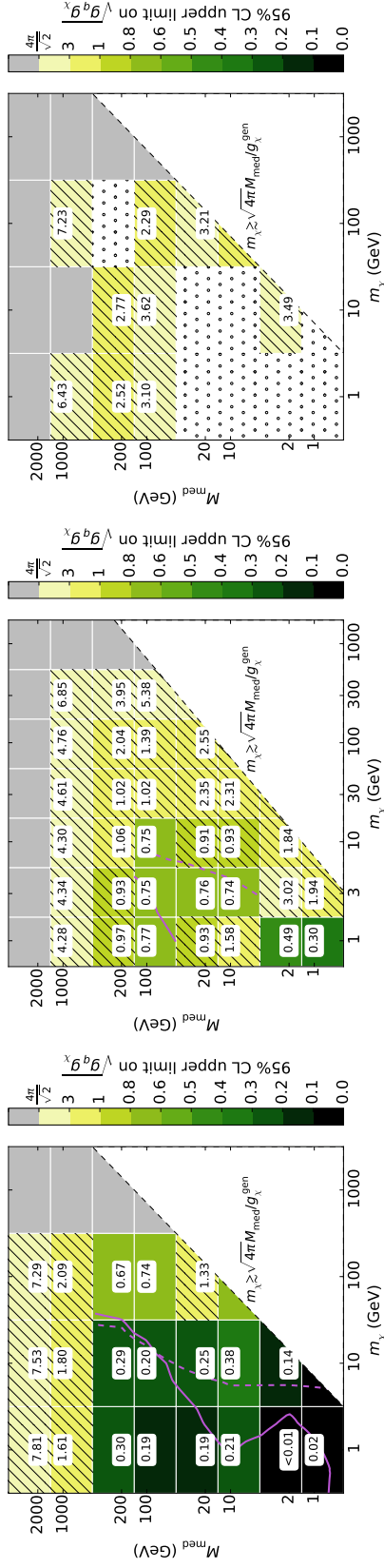
## 4.3 Comparison with Direct Detection Constraints

In figs 3-8 we also show the intercept line where constraints from direct detection experiments are equivalent to our mono- $X$  constraints. Below and to the right of the purple dotted line, direct detection constraints are stronger while above and to the left of this line, the LHC gives the stronger limit. As with the relic density contours, we do not show the intercept where it does not pass through sufficient valid data points. We use the toolset from ref [65] to convert the strongest available direct detection constraints, which are from the LUX 2013 dataset [66], onto constraints on our models.



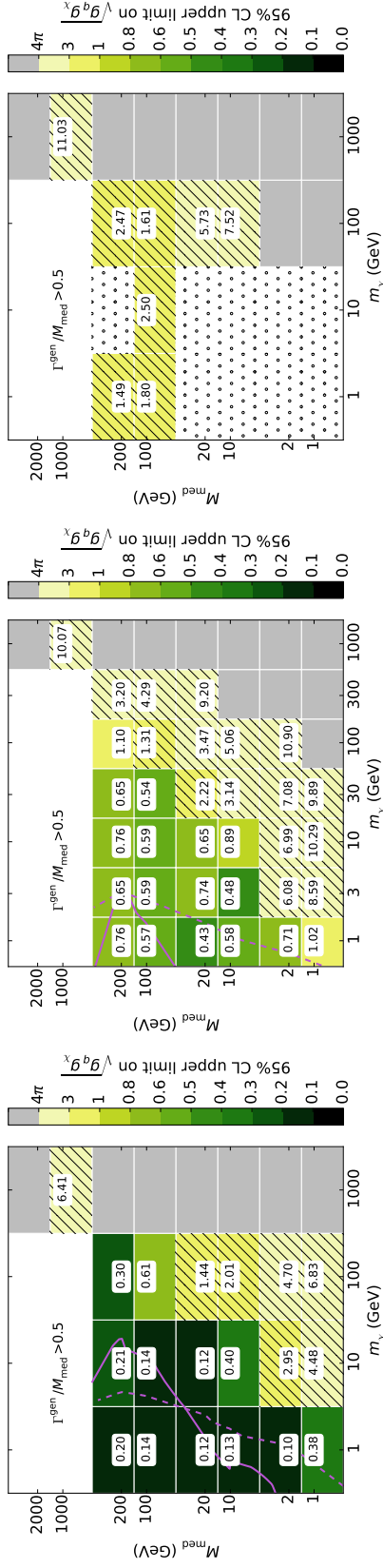


(a)  $sV$  model,  $g_X/g_q = 0.5$ , mono-jet channel. (b)  $sV$  model,  $g_X/g_q = 0.5$ , mono-Z channel. (c)  $sV$  model,  $g_X/g_q = 0.5$ , mono-W/Z channel.

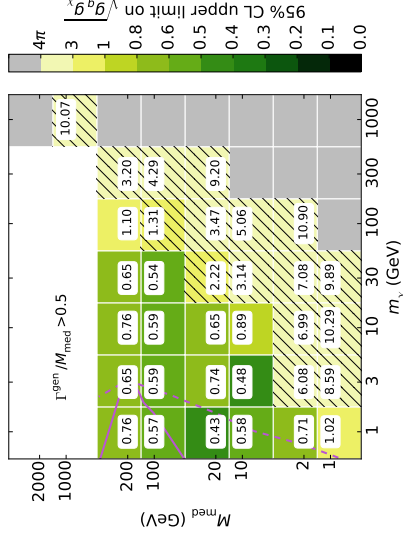


(d)  $sA$  model,  $g_X/g_q = 0.5$ , mono-jet channel. (e)  $sA$  model,  $g_X/g_q = 0.5$ , mono-Z channel. (f)  $sA$  model,  $g_X/g_q = 0.5$ , mono-W/Z channel.

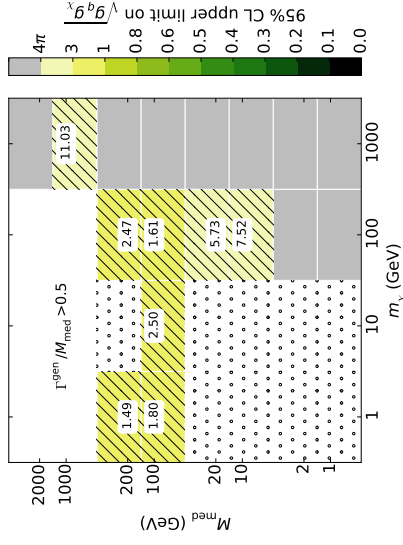
**Figure 3:** Upper limits on the coupling for the  $s$ -channel models in the mono-jet (left), mono-Z (lep) (centre) and mono-W/Z (had) (right) channels, for  $g_X/g_q = 0.5$ . The grey region represents the phase space where no meaningful limit was obtained. The hatched region represents a limit which leads to a width greater than  $M_{\text{med}}/2$ , so the validity of the calculation begins to fail. The dotted region represents phase space where insufficient statistics were available.



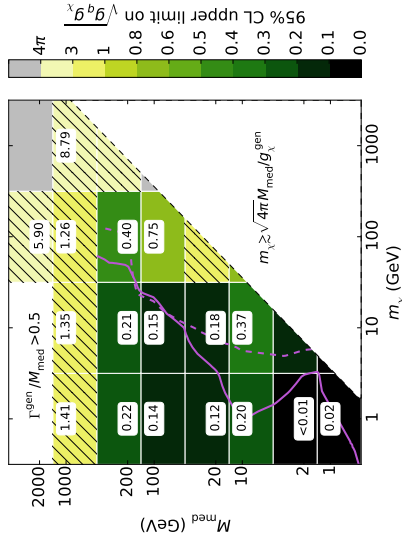
(a)  $sV$  model,  $g_\chi/g_q = 1$ , mono-jet channel.



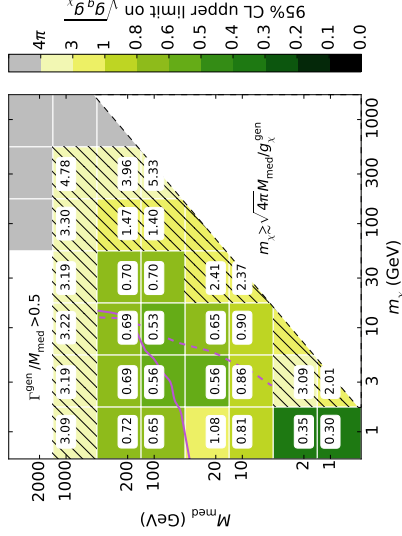
(b)  $sV$  model,  $g_\chi/g_q = 1$ , mono-Z channel.



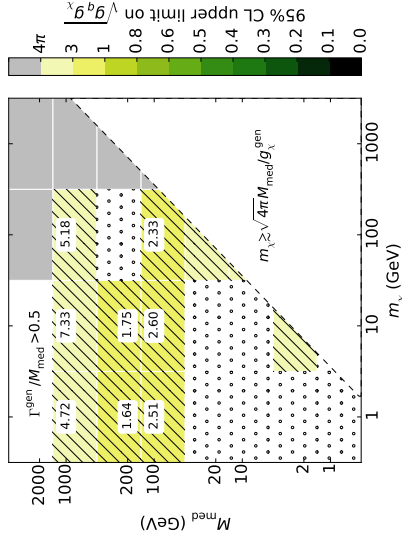
(c)  $sV$  model,  $g_\chi/g_q = 1$ , mono- $W/Z$  channel.



(d)  $sA$  model,  $g_\chi/g_q = 1$ , mono-jet channel.

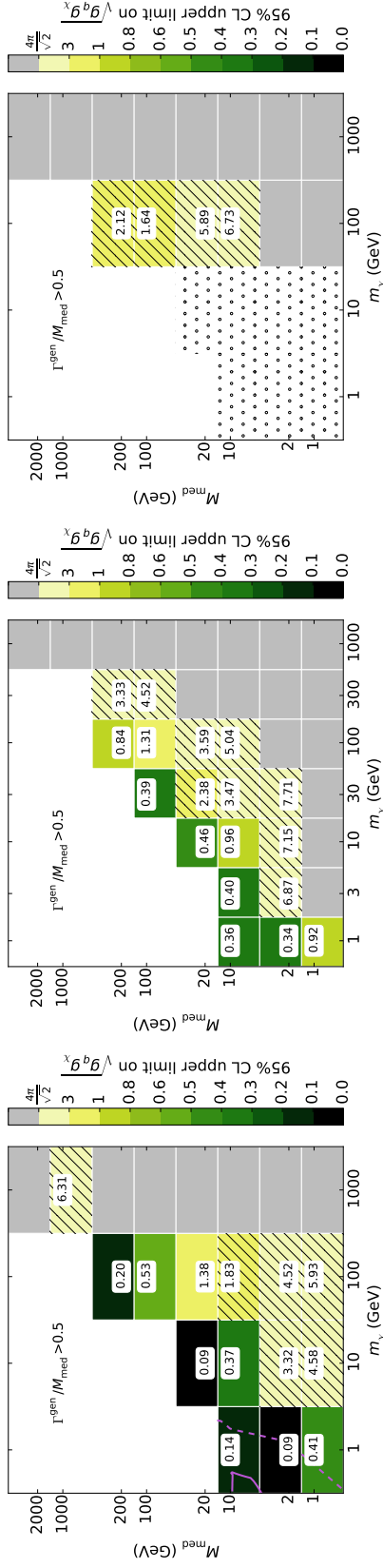


(e)  $sA$  model,  $g_\chi/g_q = 1$ , mono-Z channel.

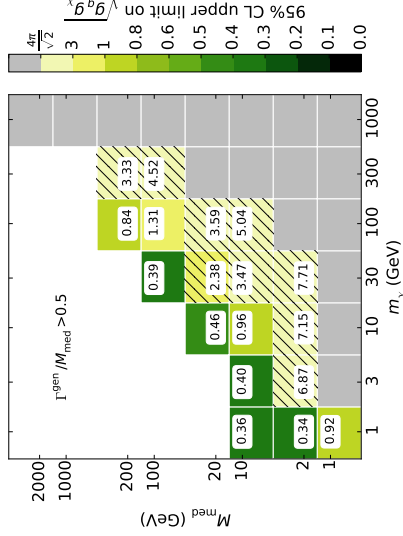


(f)  $sA$  model,  $g_\chi/g_q = 1$ , mono- $W/Z$  channel.

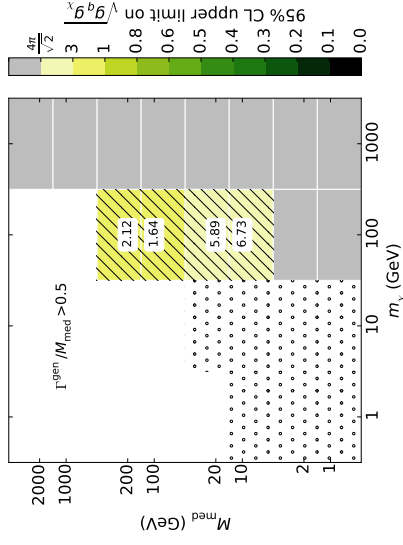
**Figure 4:** Upper limits on the couplings for the  $s$ -channel models in the mono-jet (left), mono- $Z$ (lep) (centre) and mono- $W/Z$ (had) (right) channels, for  $g_\chi/g_q = 1$ . Refer to fig. 3 for details.



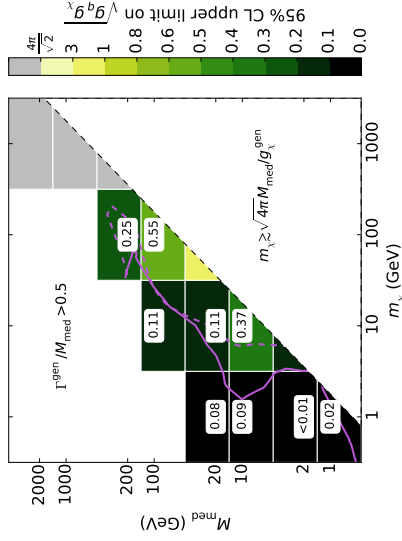
(a)  $sV$  model,  $g_\chi/g_q = 2$ , mono-jet channel.



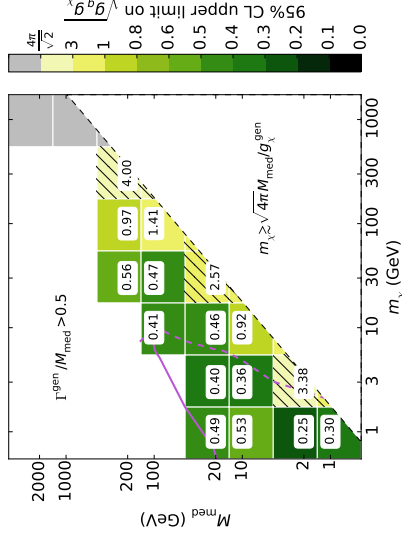
(b)  $sV$  model,  $g_\chi/g_q = 2$ , mono- $Z$  channel.



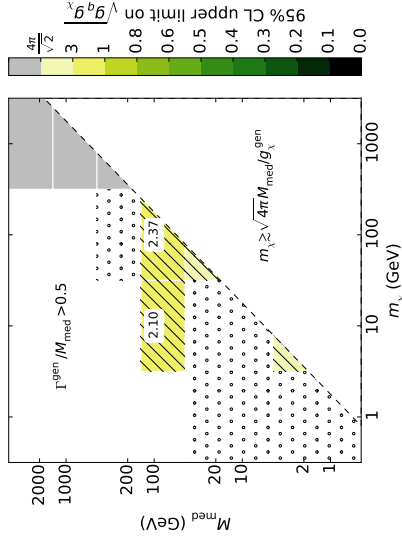
(c)  $sV$  model,  $g_\chi/g_q = 2$ , mono- $W/Z$  channel.



(d)  $sA$  model,  $g_\chi/g_q = 2$ , mono-jet channel.

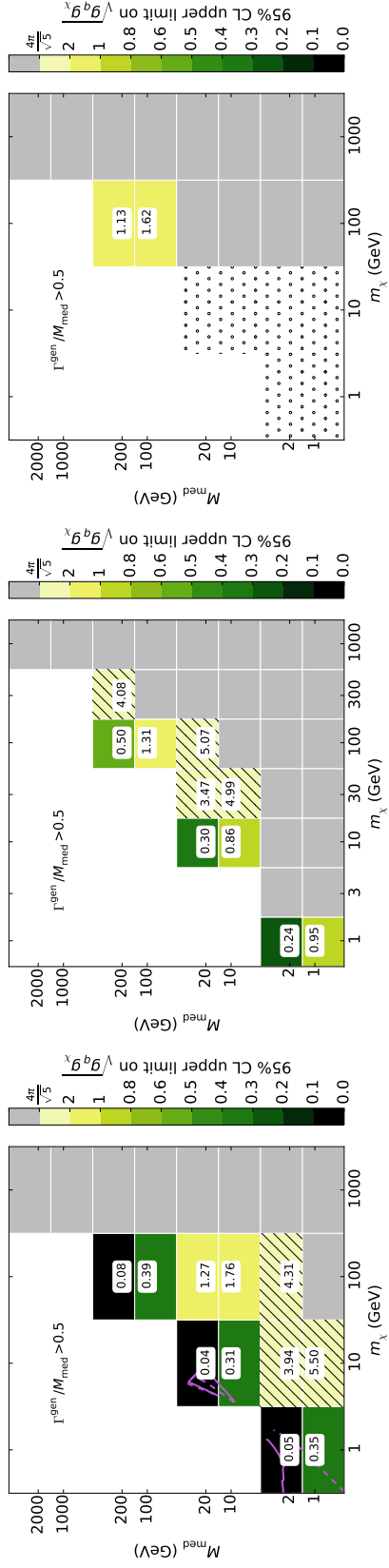


(e)  $sA$  model,  $g_\chi/g_q = 2$ , mono- $Z$  channel.



(f)  $sA$  model,  $g_\chi/g_q = 2$ , mono- $W/Z$  channel.

**Figure 5:** Upper limits on the coupling for the  $s$ -channel models in the mono-jet (left), mono- $Z$ (lep) (centre) and mono- $W/Z$ (had) (right) channels, for  $g_\chi/g_q = 2$ . Refer to fig. 3 for details.



(a)  $sV$  model,  $g_\chi/g_q = 5$ , mono-jet channel.

(b)  $sV$  model,  $g_\chi/g_q = 5$ , mono- $Z$  channel.

(c)  $sV$  model,  $g_\chi/g_q = 5$ , mono- $W/Z$  channel.

**Figure 6:** Upper limits on the coupling for the  $sV$  model in the mono-jet (left), mono- $Z$ (lep) (centre) and mono- $W/Z$ (had) (right) channels, for  $g_\chi/g_q = 5$ . Refer to fig. 3 for details.

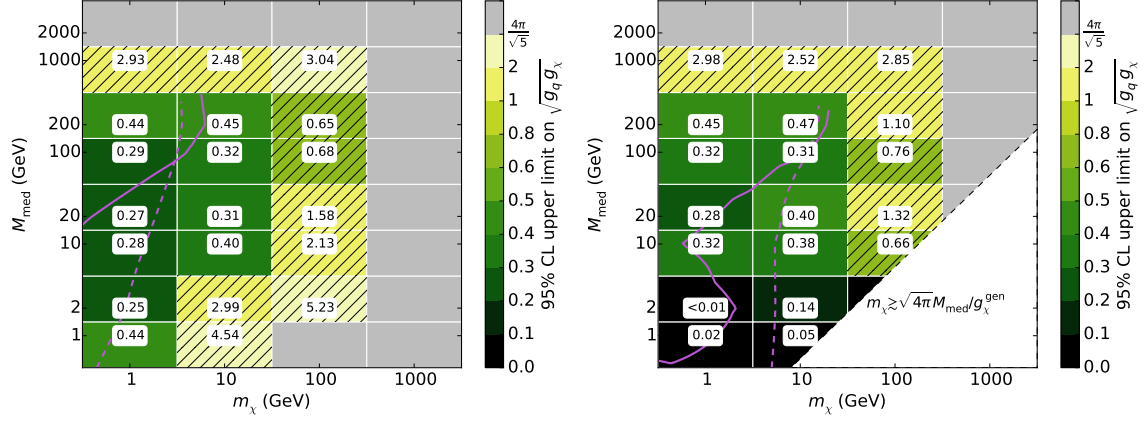


**Figure 7:** Upper limits on the coupling for the  $s$ -channel models in the mono-jet channel, for  $g_\chi/g_q = 0.2$ . Refer to fig. 3 for details.

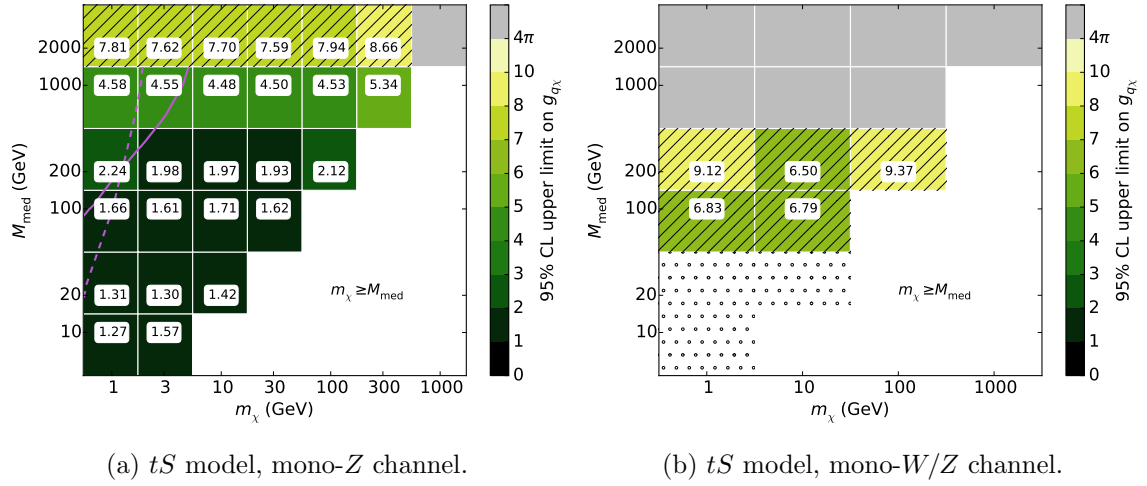


**Figure 8:** Upper limits on the coupling  $g_{q\chi}$  for the  $t$ -channel model in the mono- $Z$ (lep) (left) and mono- $W/Z$ (had) (right) channels. Refer to fig. 3 for details.

480 Compared to direct detection, the mono- $X$  collider limits perform relatively better  
 481 for the  $sA$  model than for the  $sV$  model. This is because the axial-vector coupling leads  
 482 to a suppressed scattering rate in direct detection experiments while collider searches are  
 483 relatively insensitive to the difference between the vector and axial-vector couplings. In  
 484 the non-relativistic limit, the  $tS$  model leads to a mix of both suppressed and unsuppressed  
 485 operators.

486 The direct detection constraints assume that the DM candidate under consideration  
 487 contributes 100% of the local DM density, while the mono- $X$  constraints make no assump-  
 488 tions about either the local DM density or overall abundance. In this sense the mono- $X$   
 489 limits remain useful even in those regions of phase space where they are not as strong as  
 490 or better than those from direct detection.

## 491 5 Conclusion

492 In this paper we have examined a set of three simplified dark matter models, extracting  
 493 constraints from ATLAS Run I missing energy searches featuring the associated production  
 494 of a mono-jet,  $Z(\rightarrow \text{leptons})$ , or  $W/Z(\rightarrow \text{hadrons})$ . We explored a phase space where both  
 495 the DM and mediator masses span  $\mathcal{O}(\text{GeV})$  to  $\mathcal{O}(\text{TeV})$ , and considered ratios of  $g_\chi/g_q$   
 496 of 0.2, 0.5, 1, 2 and 5 in the  $s$ -channel models. Where  $m_\chi > M_{\text{med}}$  and perturbative  
 497 unitarity isn't violated (in the  $sA$  model), we applied a reweighting procedure to account  
 498 for the MADGRAPH5 treatment of the mediator as a Breit-Wigner propagator. Rather  
 499 than setting limits in the  $M_{\text{med}} - m_{\text{DM}}$  plan for a fixed value of the coupling strength,  
 500 we instead constrained the coupling strength as a function of both  $M_{\text{med}}$  and  $m_{\text{DM}}$  in  
 501 a 3D plane. Whilst this approach necessitates the introduction of some approximations,  
 502 it also allows for a thorough examination of the interplay between the DM production  
 503 cross-section and the free parameters of the models.

504 As expected, the mono-jet channel is found to yield the strongest limits on vector and  
 505 axial-vector SM and DM couplings to a vector mediator exchanged in the  $s$ -channel. This  
 506 channel is also found to perform well for small values of  $g_\chi$ . The limits obtained in the mono-  
 507  $Z(\text{lep})$  channel, in comparison, are generally weaker by a factor of a few, while the mono-  
 508  $W/Z(\text{had})$  results are weaker again. This is partly due to our conservative estimations of the  
 509 systematic uncertainties and partly due to limited statistics resulting from a harder  $E_{\text{T}}^{\text{miss}}$   
 510 selection cut. The width effects associated with the  $t$ -channel exchange of an  $\text{SU}(2)$  doublet  
 511 scalar mediator are observed to vanish in both the mono- $Z(\text{lep})$  and mono- $W/Z(\text{had})$   
 512 channels, greatly simplifying the analysis and confirming these as straightforward and  
 513 competitive channels for future collider DM detection.

514 Where the axial-vector model is not excluded by perturbative unitarity requirements,  
 515 we find the coupling limits to be on par with those of the vector model within each anal-  
 516 ysis channel. Weaker limits are found for the  $t$ -channel model, a result of cross-section  
 517 suppression not present in the  $s$ -channel models.

518 Finally, we compared our limits to constraints from relic density and direct detection;  
 519 although each search has a different set of assumptions, this demonstrates the complemen-

520 tarity and impressive reach of simplified models as a tool for the interpretation of collider  
 521 DM searches. We eagerly await the improved constraints expected from Run II of the LHC.

## 522 6 Acknowledgements

523 A.J.B. and M.F.M. were supported by the Australian Research Council. J.G. was supported  
 524 by UNIGE and SNF (grant 200020\_156083). We thank Karl Nordström for discussions on  
 525 the cross-section reweighting, Brian Peterson and Steven Schramm for helpful discussions,  
 526 and Sean Crosby for technical support.

## 527 A Limit setting strategy

528 In this appendix we present a summary of the procedure employed to calculate the 95%  
 529 confidence level (CL) limits on the coupling parameter  $\sqrt{g_q g_\chi}$ , where this parameter can  
 530 be replaced with  $g_{q\chi}$  for the  $tS$  model, and  $M_\star$  in the validation of the mono-jet analysis.

### 531 A.1 Nominal Values

532 For each SiM, the nominal limit is calculated by taking the model-independent upper limit  
 533 on  $\sigma \times \mathcal{A} \times \epsilon$  from each analysis, dividing by the value of  $\mathcal{A} \times \epsilon$  (which is taken as a single  
 534 parameter for each point) to obtain the limiting cross section  $\sigma_{\text{lim}}$ , and rearranging eq. 2.7  
 535 to convert to a limit on the couplings. In the  $s$ -channel on-shell case, the width can be  
 536 expressed as a function of  $g_q$  and the ratio  $g_\chi/g_q$ , which simplifies the calculation. We  
 537 arrive at

$$\sqrt{g_q g_{\chi_{\text{lim}}}} = \begin{cases} \sqrt{g_q g_{\chi_{\text{gen}}}} \times (\sigma_{\text{lim}}/\sigma_{\text{gen}})^{\frac{1}{2}} & \text{if } M_{\text{med}} \geq 2m_{\text{DM}} \text{ (} s\text{-channel)} \\ \sqrt{g_q g_{\chi_{\text{gen}}}} \times (\sigma_{\text{lim}}/\sigma_{\text{gen}})^{\frac{1}{4}} & \text{if } M_{\text{med}} < 2m_{\text{DM}} \end{cases} \quad (\text{A.1})$$

538 where  $\sqrt{g_q g_{\chi_{\text{gen}}}}$  and  $\sigma_{\text{gen}}$  are the input couplings and cross-section (taken from PYTHIA 8  
 539 ), respectively.

540 The signal region in each case is chosen based on where the best ‘expected’ limit  
 541 lies, where that limit is calculated assuming that exactly the expected SM background is  
 542 observed.

### 543 A.2 Uncertainty Estimation

544 Our nominal limits rely on both  $\sigma_{\text{gen}}$  and  $\mathcal{A} \times \epsilon$  and so are subject to systematic uncertainties  
 545 which derive from our choice of signal generation procedure. For our signal samples, there  
 546 are three key sources of systematic uncertainty: the factorisation and renormalisation  
 547 scales, the strong coupling constant ( $\alpha_s$ ) and the choice of parton distribution function  
 548 (PDF).

549 We assess the impact of the factorisation and renormalisation default scales in a straight-  
 550 forward manner; by varying them simultaneously by factors of 2 (‘up’) and 0.5 (‘down’).  
 551 The systematic effects of the strong coupling constant and PDF are difficult to separate

main systematic sources	PDF/tune	factorisation and renormalisation scales	matching scale (mono-jet only)
variation ‘up’	NNPDF2.1LO + Monash tune	2	160 GeV
nominal	MSTW2008lo68cl + ATLAS UE AU2-MSTW2008LO	1	80 GeV
variation ‘down’	CTEQ6L1 + ATLAS UE AU2-CTEQ6L1	0.5	40 GeV

**Table 5:** Reading left to right, the sources of systematic uncertainty considered in this analysis. Each point in phase space is varied up or down by one of these sources, and the systematic uncertainty is then taken from the resultant changes to the acceptance and cross-section in comparison to their nominal values.

and so are treated in tandem. We assume that the systematic uncertainty introduced by  $\alpha_s$  at matrix-element level is negligible when compared to the PDF uncertainties, as demonstrated to be valid in ref. [42]. The variation of  $\alpha_s$  in conjunction with a change of PDF is done with the use of specific tunes in PYTHIA 8, which we change simultaneously with the PDF choice to estimate the uncertainty on  $\Delta\sigma_{gen}$ . The nominal choices of PDF and tune are varied ‘up’ to NNPDF2.1LO PDF + Monash tune, and ‘down’ to CTEQ6L1 PDF and ATLAS UE AU2-CTEQ6L1 tune. For the mono-jet channel, the impact of the matching scale (QCUT) is assessed in a manner similar to that of the factorisation and renormalisation scales. That is, we vary the QCUT by factors of 2 (‘up’ to 160 GeV) and 0.5 (‘down’ to 40 GeV). These systematic uncertainty sources are summarised in table 5.

The average variation in the nominal value of  $\sigma_{lim}$  (measured as a fraction of  $\sigma_{lim}$ ) resulting from each systematic source is added in quadrature and propagated to  $\sqrt{g_q g_\chi}$  to obtain the total systematic uncertainty. This process is adjusted slightly to account for the inclusion of statistical uncertainties, which are estimated conservatively by taking the 95% CL *lower* limit on  $\mathcal{A} \times \epsilon$  as calculated with the Wald approximation, i.e.  $\mathcal{A} \times \epsilon \rightarrow (\mathcal{A} \times \epsilon) - \Delta(\mathcal{A} \times \epsilon)$ . Note that the uncertainty on the luminosity is less than 3%, so is considered to be negligible in comparison to other systematic sources.

## B Validation of signal simulation and event selection procedures

### B.1 Monojet Channel

The signal generation and selection procedures for the mono-jet channel are validated via reproduction of the ATLAS limits on  $M_\star \equiv M_{med}/\sqrt{g_q g_\chi}$ , for the  $s$ -channel vector SiM. A



comparison of SR7<sup>8</sup> limits for a representative sample of mediator masses with  $m_\chi = 50$  GeV,  $\Gamma = M/8\pi$  and  $\sqrt{g_q g_\chi} = 1$  is presented in Table 6. In general, good agreement is observed between the ATLAS and reproduced limits, with a maximum difference of 12%. We note that a discrepancy of a few percent is expected given the differences in signal simulation. For example, the simplified matching procedure discussed in detail in Sec 3.1.1 introduces an additional uncertainty of approximately 25% for events with  $E_T^{\text{miss}} > 350$  GeV when compared to the approach utilised by the ATLAS mono-jet group. Further uncertainties are introduced by the jet smearing approximation used in place of a full detector simulation and by the 95% CL estimation procedure (outlined in Appendix A) used instead of a thorough HistFitter treatment. As our results are consistently more conservative than those of the ATLAS analysis, we consider our approach to be acceptable.

$M_\star^{\text{gen}}$ [TeV]	$M_\star^{95\% \text{CL}}$ [GeV] (ATLAS)	$M_\star^{95\% \text{CL}}$ [GeV] (this work)	Difference [%]
0.05	91	89	2.16
0.3	1151	1041	7.3
0.6	1868	1535	11.8
1	2225	1732	12.0
3	1349	1072	6.8
6	945	769	8.5
10	928	724	10.6
30	914	722	9.6

**Table 6:** Comparison of the 95% CL upper limits on  $M_\star$  from this work and from the ATLAS mono-jet analysis [41]. The limits are for an  $s$ -channel vector mediator model with  $m_\chi = 50$  GeV and  $\Gamma = M_{\text{med}}/8\pi$ , and for the process  $pp \rightarrow \chi\bar{\chi} + 1, 2j$  with QCUT = 80 GeV. Note that  $M_\star^{\text{gen}}$  is the input suppression scale.

## B.2 Mono- $Z(\text{lep})$ Channel

The ATLAS mono- $Z(\text{lep})$  results include an upper limit on the coupling  $g_{q\chi}$  for a  $t$ -channel SiM analogous to our  $tS$  model, and so it is this model which we use to validate our signal generation and selection procedures. Note that the following differences exist: the ATLAS model includes just two mediators ( $up$ - and  $down$ -type) where we consider six, the DM particle is taken to be Majorana where we assume Dirac, and the couplings  $g_{t,b\chi}$  are set to zero where we have universal coupling to all three quark generations.

Table 7 shows the 95% CL upper limits on  $g_{q\chi}$  that we calculate using our own generation procedure (and the values in table 3), compared with the limits taken from the ATLAS analysis. Also shown is the difference as a percentage of the ATLAS limit. We see reasonable agreement; most of the 11 points in parameter space are within 10% of the ATLAS limits, and all are within 26%. Additionally, our results are consistently more

<sup>8</sup>We use this signal region as it is the only one for which ATLAS limits are provided.

$m_\chi$ [GeV]	$M_{\text{med}}$ [GeV]	$g_{q\chi}^{95\% \text{CL}}$ (ATLAS)	$g_{q\chi}^{95\% \text{CL}}$ (this work)	Difference [%]
10	200	1.9	2.0	5.3
	500	2.8	3.2	14.3
	700	3.5	4.4	25.7
	1000	4.5	5.2	15.6
200	500	3.4	4.0	17.6
	700	4.2	4.5	7.1
	1000	5.2	5.3	1.9
400	500	5.5	5.7	3.6
	700	6.1	6.5	6.6
	1000	7.2	7.4	2.8
1000	1200	23.3	24.1	3.4

**Table 7:** Comparison of the 95% CL upper limit on  $g_{q\chi}$  from this work and from the ATLAS mono- $Z(\text{lep})$  analysis [47]. The limits are for a variant of the  $t$ -channel scalar mediator model with Majorana Dark matter for the process  $pp \rightarrow \chi\bar{\chi} + Z(\rightarrow e^+e^-/\mu^+\mu^-)$ .

conservative, which again is to be expected given the less sophisticated nature of our generation procedure. As in the case of the mono-jet validation, the differences stem from the use of  $p_T$  smearing applied to the leptons (rather than a full reconstruction simulation) and from the simplified treatment of systematics; we also obtained  $\sigma \times \mathcal{A} \times \epsilon$  independently.

### B.3 Mono- $W/Z(\text{had})$ Channel

The event generation and selection procedures for the mono- $W/Z(\text{had})$  channel are validated via reproduction of the ATLAS limits on  $M_\star$  for the D5 and D9 effective operators with  $m_\chi = 1$  GeV. We see agreement within 12.5% and 7.4% respectively, where the ATLAS limits are consistently stronger, as shown in table B.3. The relative sizes of the discrepancies are expected given that only low- $E_T^{\text{miss}}$  limits are available for the D5 operator while we use the high- $E_T^{\text{miss}}$  signal region in our recast. Note that a general discrepancy of a few percent is expected for both operators for the reasons discussed in sections B.1 and B.2, and also because we use a cut-and-count approach while the ATLAS limits are extracted using a shape-fit. Furthermore, the ATLAS limits are quoted at 90% CL while ours are calculated at 95% CL.

## References

- [1] ATLAS Collaboration, *Search for new phenomena with the monojet and missing transverse momentum signature using the ATLAS detector in  $\sqrt{s} = 7$  TeV proton-proton collisions*, *Phys. Lett. B* (2011), arXiv:1106.5327.

EFT operator	$m_\chi$ [GeV]	$M_\star^{90\%CL}$ [GeV] (ATLAS)	$M_\star^{95\%CL}$ [GeV] (this work)	Difference [%]
D9	1	2400	2221	7.4
D5	1	570	499	12.5

**Table 8:** Comparison of the 95% CL upper limits on  $M_\star$  from this work and from the ATLAS mono- $W/Z$ (had) analysis [48]. The limits are for the process  $pp \rightarrow \chi\bar{\chi} + W/Z (\rightarrow jj)$ .

- [2] ATLAS Collaboration, *Search for New Phenomena in Monojet plus Missing Transverse Momentum Final States using  $10 \text{ fb}^{-1}$  of  $pp$  collisions at  $\sqrt{s}=8 \text{ TeV}$  with the ATLAS detector at the LHC*, 2012, ATLAS-CONF-2012-147.
- [3] CMS Collaboration, *Search for new physics in monojet events in  $pp$  collisions at  $\sqrt{s} = 8 \text{ TeV}$* , 2013, CMS-PAS-EXO-12-048.
- [4] M. R. Buckley, *Using Effective Operators to Understand CoGeNT and CDMS-Si*, *Phys.Rev. D* 88, 055028 (2013), arXiv:1308.4146.
- [5] ATLAS Collaboration, *Search for new phenomena with mono-jet plus missing transverse energy signature in  $pp$  collisions at  $\sqrt{s}=8 \text{ TeV}$  with the ATLAS detector*, 2012, ATL-COM-PHYS-2012-1211.
- [6] N. Bell et al., *Searching for Dark Matter at the LHC with a Mono-Z*, *Phys.Rev. D* 86, 096011 (2012), arXiv:1209.0231.
- [7] N. Zhou, D. Berge, and D. Whiteson, *Mono-everything: combined limits on dark matter production at colliders from multiple final states*, *Phys.Rev. D* 87, 095013 (2013), arXiv:1302.3619.
- [8] M. Cahill-Rowley et al., *Complementarity and Searches for Dark Matter in the pMSSM*, SLAC-PUB-15450 (2013), arXiv:1305.6921.
- [9] ATLAS Collaboration, *Further search for supersymmetry at  $\sqrt{s} = 7 \text{ TeV}$  in final states with jets, missing transverse momentum and isolated leptons with the ATLAS detector*, *Phys.Rev. D* 86, 092002 (2012), arXiv:1208.4688.
- [10] ATLAS Collaboration, *Search for squarks and gluinos with the ATLAS detector in final states with jets and missing transverse momentum using  $4.7 \text{ fb}^{-1}$  of  $\sqrt{s} = 7 \text{ TeV}$  proton-proton collision data*, *Phys.Rev. D* 87, 012008 (2013), arXiv:1208.0949.
- [11] ATLAS Collaboration, *Search for pair-produced third-generation squarks decaying via charm quarks or in compressed supersymmetric scenarios in  $pp$  collisions at  $\sqrt{s} = 8 \text{ TeV}$  with the ATLAS detector*, *Phys.Rev. D* 90, 052008 (2014), arXiv:1407.0608.
- [12] ATLAS Collaboration, *Search for squarks and gluinos with the ATLAS detector in final states with jets and missing transverse momentum using  $\sqrt{s} = 8 \text{ TeV}$  proton-proton collision data*, *JHEP* 09 (2014) 146, arXiv:1405.7875.
- [13] H. Dreiner et al., *Contact Interactions Probe Effective Dark Matter Models at the LHC*, *Europhys.Lett.* (2013), arXiv:1303.3348.

- [14] J. Goodman et al., *Gamma Ray Line Constraints on Effective Theories of Dark Matter*, *Nucl.Phys.* (2011), arXiv:1009.0008.
- [15] G. Busoni et al., *On the Validity of the Effective Field Theory for Dark Matter Searches at the LHC*, *Phys.Lett.* (2014), arXiv:1307.2253.
- [16] G. Busoni et al., *On the Validity of the Effective Field Theory for Dark Matter Searches at the LHC, Part II: Complete Analysis for the s-channel*, *JCAP* 1406:060 (2014), arXiv:1402.1275.
- [17] G. Busoni et al., *On the Validity of the Effective Field Theory for Dark Matter Searches at the LHC Part III: Analysis for the t-channel*, *JCAP* 09 (2014) 022, arXiv:1405.3101.
- [18] Oliver Buchmueller, Matthew J. Dolan, Sarah A. Malik and Christopher McCabe, *Characterising dark matter searches at colliders and direct detection experiments: Vector mediators*, 2014, arXiv:1407.8257.
- [19] J. Kumar and D. Marfatia. *Matrix element analyses of dark matter scattering and annihilation*, *Phys.Rev.* (2013), arXiv:1305.1611.
- [20] G. Jungman et al., *Supersymmetric dark matter*, *Phys.Rept.* (1996).
- [21] P. J. Fox et al., *Missing Energy Signatures of Dark Matter at the LHC*, *Phys.Rev.* (2012), arXiv:1109.4398.
- [22] P. J. Fox, R. Harnik, R. Primulando, and C-T. Yu, *Taking a Razor to Dark Matter Parameter Space at the LHC*, *Phys.Rev.* (2012), arXiv:1203.1662.
- [23] M. Papucci, A. Vichi, and K. M. Zurek, *Monojet versus rest of the world I: t-channel Models*, *JHEP* (2014), arXiv:1402.2285.
- [24] Y. Bai, P. J. Fox, and R. Harnik, *The Tevatron at the Frontier of Dark Matter Direct Detection*, *JHEP* (2010), arXiv:1005.3797.
- [25] J. Goodman et al., *Constraints on Dark Matter from Colliders*, *Phys.Rev. D* 82, 116010 (2010), arXiv:1008.1783.
- [26] P. J. Fox, R. Harnik, J. Kopp, and Y. Tsai, *LEP Shines Light on Dark Matter*, *Phys.Rev.* (2011), arXiv:1103.0240.
- [27] M. L. Graesser, I. M. Shoemaker, and L. Vecchi, *A Dark Force for Baryons*, 2011, arXiv:1107.2666.
- [28] H. An and F. Gao, *Fitting CoGeNT Modulation with an Inelastic, Isopin-Violating  $Z'$  Model*, 2011, arXiv:1108.3943.
- [29] CMS Collaboration, *Search for narrow resonances using the dijet mass spectrum in pp collisions at  $\sqrt{s} = 8\text{TeV}$* , *Phys.Rev.* (2013), arXiv:1302.4794.
- [30] ATLAS Collaboration, *Search for high-mass resonances decaying to dilepton final states in pp collisions at  $\sqrt{s} = 7\text{-TeV}$  with the ATLAS detector*, *JHEP* (2012), arXiv:1209.2535.
- [31] P. Harris, V. V. Khoze, M. Spannowsky and C. Williams, *Constraining Dark Sectors at Colliders: Beyond the Effective Theory Approach*, *Phys.Rev.* (2015), arXiv:1411.0535.
- [32] CMS Collaboration. *Search for new physics in monojet events in pp collisions at  $\sqrt{s} = 8\text{TeV}$* , 2013, CMS-PAS-EXO-12-048.
- [33] ATLAS Collaboration. *Search for New Phenomena in Monojet plus Missing Transverse*

- 686 *Momentum Final States using 10 fb<sup>1</sup> of pp collisions at  $\sqrt{s} = 8$  TeV with the ATLAS*  
687 *detector at the LHC*, 2012, ATLAS-CONF-2012-147.
- 688 [34] J. Kumar and D. Marfatia, *Matrix element analyses of dark matter scattering and*  
689 *annihilation*, *Phys.Rev.* (2013), arXiv:1305.1611.
- 690 [35] D. Alves et al., *Simplified Models for LHC New Physics Searches*, *J.Phys.* (2012),  
691 arXiv:1105.2838.
- 692 [36] P. A. R. Ade *et al.* [Planck Collaboration], *Astron. Astrophys.* **571**, A16 (2014)  
693 [arXiv:1303.5076 [astro-ph.CO]].
- 694 [37] G. Busoni, A. De Simone, T. Jacques, E. Morgante and A. Riotto, *Making the Most of the*  
695 *Relic Density for Dark Matter Searches at the LHC 14 TeV Run*, *JCAP* 03 (2015) 022,  
696 arXiv:1410.7409.
- 697 [38] CMS Collaboration. *Search for new physics in monojet events in pp collisions at  $\sqrt{s} = 8$*   
698 *TeV*, 2013, CMS-PAS-EXO-12-048.
- 699 [39] ATLAS Collaboration. *Search for New Phenomena in Monojet plus Missing Transverse*  
700 *Momentum Final States using 10 fb<sup>1</sup> of pp collisions at  $\sqrt{s} = 8$  TeV with the ATLAS*  
701 *detector at the LHC*, 2012, ATLAS-CONF-2012-147.
- 702 [40] ATLAS Collaboration. *Further search for supersymmetry at  $\sqrt{s} = 7$  TeV in final states with*  
703 *jets, missing transverse momentum and isolated leptons with the ATLAS detector*, *Phys.Rev.*  
704 (2012), arXiv:1208.4688.
- 705 [41] ATLAS Collaboration. *Search for new phenomena in final states with an energetic jet and*  
706 *large missing transverse momentum in pp collisions at  $\sqrt{s} = 8$  TeV with the ATLAS*  
707 *detector*, 2015, arXiv:1502.01518
- 708 [42] S. Schramm, *Searching for Dark Matter with the ATLAS Detector in Events with an*  
709 *Energetic Jet and Large Missing Transverse Momentum*, 2015, CERN-THESIS-2015-038.
- 710 [43] A. Cooper-Sarkar. *PDFs for the LHC*, 2011, arXiv:1107.5170.
- 711 [44] ATLAS Collaboration. *Search for dark matter candidates and large extra dimensions in*  
712 *events with a jet and missing transverse momentum with the ATLAS detector*, 2013,  
713 CERN-PH-EP-2012-210, arXiv:1210.4491.
- 714 [45] P. J. Fox et al. *Missing Energy Signatures of Dark Matter at the LHC*, *Phys. Rev.*, 2012.
- 715 [46] N. Bell, J. Dent, T. Jacques, and T. Weiler. *W/Z Bremsstrahlung as the Dominant*  
716 *Annihilation Channel for Dark Matter*, *Phys. Rev.*, 2011.
- 717 [47] ATLAS Collaboration. *Search for dark matter in events with a Z boson and missing*  
718 *transverse momentum in pp collisions at  $\sqrt{s} = 8$  TeV with the ATLAS detector*, *Phys.Rev.D*  
719 **90** (2014) 012004, arXiv:1404.0051.
- 720 [48] ATLAS Collaboration. *Search for dark matter in events with a hadronically decaying W or Z*  
721 *boson and missing transverse momentum in pp collisions at  $\sqrt{s} = 8$  TeV with the ATLAS*  
722 *detector*, *Phys. Rev. Lett.* **112** (2014) 041802, arXiv:1309.4017.
- 723 [49] J. Alwall /emphet al.. *The automated computation of tree-level and next-to-leading order*  
724 *differential cross sections, and their matching to parton shower simulations*, *JHEP07* (2014)  
725 079, arXiv:1405.0301.
- 726 [50] A. D. Martin, W. J. Stirling, R. S. Thorne, G. Watt, *Parton distributions for the LHC*,  
727 *Eur.Phys.J.C63*, (2009), 189-285, arXiv:0901.0002.

- [51] ATLAS Collaboration. *Summary of ATLAS Pythia8 tunes*, 2012, ATL-PHYS-PUB-2012-003.
- [52] G. Blanger, F. Boudjema, A. Pukhov and A. Semenov, *Comput. Phys. Commun.* **192**, 322 (2015) doi:10.1016/j.cpc.2015.03.003 [arXiv:1407.6129 [hep-ph]].
- [53] D. Abercrombie et al. *Dark Matter Benchmark Models for Early LHC Run-2 Searches: Report of the ATLAS/CMS Dark Matter Forum*, arXiv:1507.00966.
- [54] M. Baak et al. *HistFitter software framework for statistical data analysis*, *Eur.Phys.J.C* (2015), arXiv:1410.1280.
- [55] J. Abdallah et al. *Simplified Models for Dark Matter Searches at the LHC*, *Phys. Dark Uni.* 9-10 (2015) 8-23, arXiv:1506.03116.
- [56] J. Abdallah et al. *Simplified Models for Dark Matter and Missing Energy Searches at the LHC*, (2014), arXiv:1409.2893.
- [57] T. Jacques and K. Nordstrom, *Mapping monojet constraints onto Simplified Dark Matter Models*, *JHEP* 06 (2015) 142, arXiv:1502.05721.
- [58] T. Sjstrand et al. *An Introduction to PYTHIA 8.2*, *Comput. Phys. Comm.* 191 (2015) 159-177, arXiv:1410.3012.
- [59] R. M. Godbole, G. Mendiratta and T. M. P. Tait, *A Simplified Model for Dark Matter Interacting Primarily with Gluons*, *JHEP* 08 (2015) 064, arXiv:1506.01408.
- [60] ATLAS Collaboration, *Search for dark matter produced in association with a hadronically decaying vector boson in pp collisions at  $\sqrt{s} = 13$  TeV with the ATLAS detector at the LHC*, ATLAS-CONF-2015-080 (2015).
- [61] M. L. Mangano et al. *Matching matrix elements and shower evolution for top-quark production in hadronic collisions*, *JHEP* 01 (2007), hep-ph/0611129.
- [62] ATLAS Collaboration, *Performance of jet substructure techniques for large- $R$  jets in proton-proton collisions at  $\sqrt{s} = 7$  TeV using the ATLAS detector*, *JHEP* 09 (2013) 076, arXiv:1306.4945.
- [63] M. Cacciari, G. P. Salam and G. Soyez, *FastJet user manual*, arXiv:1111.6097.
- [64] N. F. Bell et al, *Dark matter at the LHC: EFTs and gauge invariance*, *Phys. Rev. D* 92 (2015) 053008, arXiv:1503.07874.
- [65] M. Cirelli, E. Del Nobile and P. Panci, *Tools for model-independent bounds in direct dark matter searches*, *JCAP*1310 (2013) 019, arXiv:1307.5955.
- [66] D. S. Akerib et al. [LUX Collaboration], *First results from the LUX dark matter experiment at the Sanford Underground Research Facility*, *Phys. Rev. Lett.* 112 (2014) 091303, arXiv:1310.8214.
- [67] G. Aad et al. [ATLAS Collaboration], *Search for new phenomena in the dijet mass distribution using  $p-p$  collision data at  $\sqrt{s} = 8$  TeV with the ATLAS detector*, *Phys. Rev. D* 91 (2015) 5, 052007, arXiv:1407.1376.
- [68] T. Aaltonen et al. [CDF Collaboration], *Search for new particles decaying into dijets in proton-antiproton collisions at  $s^{1/2} = 1.96$ -TeV*, *Phys. Rev. D* 79 (2009) 112002, arXiv:0812.4036
- [69] V. Khachatryan et al. [CMS Collaboration], *Search for resonances and quantum black holes using dijet mass spectra in proton-proton collisions at  $\sqrt{s} = 8$  TeV*, *Phys. Rev. D* 91 (2015) 5, 052009, arXiv:1501.04198

- 770 [70] H. An, X. Ji and L. T. Wang, *Light Dark Matter and  $Z'$  Dark Force at Colliders*, *JHEP*  
771 1207 (2012) 182, arXiv:1202.2894.
- 772 [71] N. F. Bell, Y. Cai and R. K. Leane, *Mono- $W$  Dark Matter Signals at the LHC: Simplified*  
773 *Model Analysis*, *JCAP* 1601 (2016) 01, 051, arXiv:1512.00476.
- 774 [72] A. DiFranzo, K. I. Nagao, A. Rajaraman, and T. M. P. Tait *Simplified Models for Dark*  
775 *Matter Interacting with Quarks*, *JHEP* 11 (2013) 014, arXiv:1308.2679.
- 776 [73] M. R. Buckley, D. Feld, and D. Goncalves, *Scalar Simplified Models for Dark Matter*, *Phys.*  
777 *Rev. D* 91 (2015) 015017, arXiv:1410.6497.